FULL RESEARCH ARTICLE

Feasibility of using bio-mimicking fish scale textures in LPBF for water drag-reducing surfaces

Alessandro Scarpellini[1] · Paolo Schito[1] · Ali Gökhan Demir[1]

Abstract

In this work, bio-mimicking fish scale textures are produced by LPBF and AlSi7Mg0.6 powder to reduce drag forces on nautical components. For this purpose, a surface texture inspired by the European bass skin was modelled and parametrized. Textures were applied over the external surface of purpose-designed specimens. Additive manufacturing quality of textures was assessed using focus variation microscopy to examine surface roughness as well as geometrical errors. Once the feasibility of producing the desired bio-mimicking surfaces was confirmed, the designed surface patterns were analysed in the computation fluid dynamics modelling environment. The behaviour of the surfaces was characterized in terms of drag force generated over a fixed dimension plate model. The most promising configuration was further investigated in a sensitivity analysis where variations in main stream velocity and in surface roughness are applied. Drag reduction was related to the lowering of the viscous component and was found to be in the order of 1–2%, with respect to a smooth surface, for free stream velocity of 2.5–5 m s^{-1} and average roughness smaller than the as-built condition. The results confirm that the modelled surfaces can be reproduced with sufficient geometrical fidelity, showing great promise for drag-reducing metallic components produced by additive manufacturing.

Keywords Bio-inspired surfaces · Surface texturing · Fish skin · CFD modelling · Functional surfaces

List of symbols

l	Scale radius, mm
h_s	Scale maximum height, mm
α	Scale midsection nucleation angle, deg
β	Scale midsection base angle, deg
γ	Scale midsection upper angle, deg
dl	Scales longitudinal distance, mm
dc	Scales transversal distance, mm
ρ	Fluid density, kg m^{-3}
k	Turbulent kinetic energy, J kg^{-1}
ω	Turbulent dissipation rate, s^{-1}
F_p	Pressure component of drag force, mN
F_v	Viscous component of drag force, mN
F_d	Drag force, mN
U_∞	Main stream velocity, m s^{-1}
A_{front}	Projected frontal area impacting the stream orthogonally, mm^2
C_v	Viscous drag coefficient, –
C_d	Drag coefficient, –
ΔC_v	Viscous drag coefficient variation, –
ΔC_d	Drag coefficient variation, –
k_s	Equivalent sand grain diameter, μm
R_a	Average profile roughness, μm
Δpv_{meas}	Mean peak to valley distance, μm
Δpv_{theo}	Theoretical peak to valley distance, μm
$\Delta(\Delta pv)$	Peak to valley distance error, μm
R_R	Roughness Reynolds number, –
U	Undisturbed velocity at maximum roughness height, m s^{-1}
μ	Fluid dynamic viscosity, Pa s

✉ Ali Gökhan Demir
    aligokhan.demir@polimi.it

1   Department of Mechanical Engineering, Politecnico Di Milano, Via La Masa 1, 20156 Milan, Italy

1 Introduction

The reduction of CO_2 emissions has been a key target in the marine industry since the International Maritime Organization (IMO), through the Marine Environment Protection Committee (MEPC), published a CO_2 analysis in the shipbuilding and marine industry (2008). The main priority has been on innovative production and solutions to reduce the CO_2 footprint [1]. Ship fuel consumption is first among the

causes that produce carbon dioxide emissions and for this reason energy dissipation due to fluid dynamic resistance in air and water must be minimized as well as mass, by means of high strength to weight ratio materials (e.g. Al-alloys). Drag force exerted on floating bodies such as ships or submarines imposes large costs due to the increase of the fuel consumption and so emissions, limited by standards. Friction loss is a major problem also in pipeline industries, which are used for liquid transport; it leads to an increase in power required for hydraulic pumps and so operational costs [2]. For vessels, the main components of ship resistance consist of wave, pressure and frictional resistances. With ship's hull form optimization techniques, the wave and the pressure components could be less than 20% of the total drag in most modern ships [3]. Therefore, the required innovation concerns reduction of the remaining frictional drag.

A plain smooth surface, as reported by Liravi et al. [2], is found to be not optimal in energy dissipation, due to consistent adhesion of fluid and consequent enhanced internal shear stresses between one layer of fluid and the other, up to the not disturbed fluid. Streamwise oriented streaks studied by Pujals et al. [4] are effective in drag reduction. However, it is found more common in literature the development of surface geometry that mimics shark skin allowing drag reduction with respect to a smooth surface [5–7]. Coherently, also surface textures capabilities are faced [8–10]. Drag reduction studies frequently refer to their results in terms of percentage of reduction with respect to the untreated, unaffected, smooth or reference condition. Solutions are frequently inspired by existing natural cases that through natural selection have resulted in optimized geometries. Such solutions appear to be widely open to sensible adaptability to human applications, by modelling, simulation, experimentation and optimization. Fu et al. [5] underline the interesting fact that superimposition of multiple solutions on the same application may produce greater benefits than the sum of the improvements obtained by each solution independently considered. This reveals that enormous potential is available due to interactions between drag-reducing factors involved in the same application. Additive Manufacturing (AM), thanks to its wide design potential, allows complex geometrical features to be reproduced easily in the final shape, thus avoiding expensive post processing.

Fish scale inspired surfaces are in general capable of generating local micro-vortices effectively reducing shear stresses, as obtained by shark skin inspired riblets [5–7]. Different techniques are adopted and introduced as simplified but parametrized models of natural cases. The "streak" generation technique is characterized by vortices generated by different speed streams (streaks) disposed alternatively beside each other [4, 11]. The presence of streaks is described as providing a stabilizing effect on the disturbances that occur on the body surface, this reduces the turbulence and so amplifies the laminar portion of the boundary layer, retarding the transition to turbulent flow [4]. Streaks related studies appear promising despite the fewer works in the literature, that is much richer in shark skin inspired ones [12–17], as well as modelling of fish bodies to assess fluid interaction capabilities [18]. The regular arrangement of streaks is known as capable of stabilising the laminar steady state and delaying the transition to turbulence [11]. A model based on a fish scale pattern is studied by Muthuramalingam et al. [11] with streak generation. Streak formation was attributed to the interaction of the scale geometry with fluid, which ends up to be arranged in a span-wise direction in the same pattern as the rows of the laterally overlapping scales. Fluid speed corridors have been experimentally shown on both numerical simulations and on a real fish body, painted with pigmented oil. Drag reductions of the order of 4% compared with a smooth surface are obtained from this model through numerical simulations. By having the height of the scales smaller or equal to 0.1 mm, Muthuramalingam et al. [11] described European sea bass scales as acting like roughness elements which are placed well inside the boundary layer to produce steady low and high-speed streaks without inducing transition to turbulence. The combination of design freedom provided by additive manufacturing and functional surfaces can open up several possibilities [19]. Although the surface quality, properties, and finishing of LPBF produced alloys has been widely studied [20–23], the generation of functional surface textures through this process has not received the same amount of attention [24, 25]. Indeed, a comprehensive study comprised of assessing modelling and manufacturing issues is an open field that requires further attention. To the authors' knowledge, no previous work has yet assessed the feasibility of producing digitally designed drag-reducing surfaces via LPBF.

Accordingly, this work investigates in a systematic way the parametric CAD modelling, additive manufacturing and CFD analysis of bio-mimicking fish skin surfaces for water drag reduction. The surface pattern was inspired by the European bass fish. The designed surfaces were applied to curved surfaces and produced by LPBF using AlSi7Mg0.6. Surface roughness and geometrical deviations were analyzed via focus variation microscopy. The CFD modelling assessed the steady swimming conditions representative of a Moth-class sail boat. A sensitivity analysis was further conducted to understand the influence of surface roughness and sailing speed.

2 Parametrization of the European bass scales

The definition of the texturing of the bulb surface requires an analysis of the geometry of a real fish. The geometry of the fish scales needs to be determined in order to be designed on a complex surface. Literature studies related to the study

of sea bass scales are available [11] and allow the scales to be parametrized and put on the surface of the rudder bulb. In the sections below the parametrization and the modelling of the fish scales will be presented (Fig. 1).

2.1 Determination of the surface design parameters

The surface texturing was based on the actual scales of the European bass in terms of dimensions and periodic repetitions in space. The single scale was modelled as a half circle, linearly growing in thickness and triangular in vertical section. Starting from the midsection (Fig. 2a, section A–A), the scale was drawn as a triangle, with base length l (equal to the circle's radius), height h_s as the maximum scale thickness and the three internal angles with α as the main "scale angle", β, and γ. The pattern must see the scales oriented according to the longitudinal axis of the considered carrying body for the growing thickness of the scales themselves and transversally with the "scale diameter" (as it corresponds to the origin position of α). The longitudinal distance between neighbour-row scales was denoted by dl, while between aligned non row-neighbouring scales it was set to $2 \times$ dl. The transversal spacing between transversally aligned scales is denoted by dc, while between non-transversally aligned scales the spacing was set to $0.5 \times$ dc. To model a single scale, the midsection triangle is taken as the generative portion for the solid obtained by revolution around the vertical axis (Fig. 2b). The solid was then cut according to the inner inclination to obtain the single scale (Fig. 2c, d). The scale pattern was obtained by means of a linear pattern operation on a single scale and on rows (Dassault Systèmes Solidworks environment). Measured sea bass scales [11] are inclined at 3° and have a maximum thickness of 0.1 mm. As a reference geometry, these values are taken as $\alpha = 3°$ and $h_s = 0.1$ mm. By having l fixed at approximately 2 mm, the scale's middle section geometry was fixed ($\beta = 47°$, $\gamma = 130°$) and from which all the other parameters followed. The pattern can be generically determined by dl and dc since scales are considered to be distributed only in two directions (i.e. same fixed vertical position). Their reference values, extrapolated from the work of Muthuramalingam et al. [11], are found to be approximately dl = 0.9 mm and dc = 6 mm, respectively.

2.2 Parametric surface design for LPBF and CFD studies

The first objective was to design parametric scaled surfaces to reduce water drag at the same Reynolds number ($U_\infty = 2.5$ m s^{-1}). The parametric design considered the successive manufacturability avoiding excessively thin sections (< 0.1 mm) and large overhangs (> 1 mm). Two parameters were varied for the scale geometry (α and l) and two for the pattern (dl and dc). Two levels were chosen for each parameter and all combinations were analysed. The scale base angle β was kept fixed at 47° as from the reference scale shape. With a constant value of β, different scale geometries varying α and scale radius (or length) l were assessed (Table 1). The low levels of the parameters were chosen referring to [11], while the high levels were set 50% higher than low levels. It was preferred to test bigger geometries in
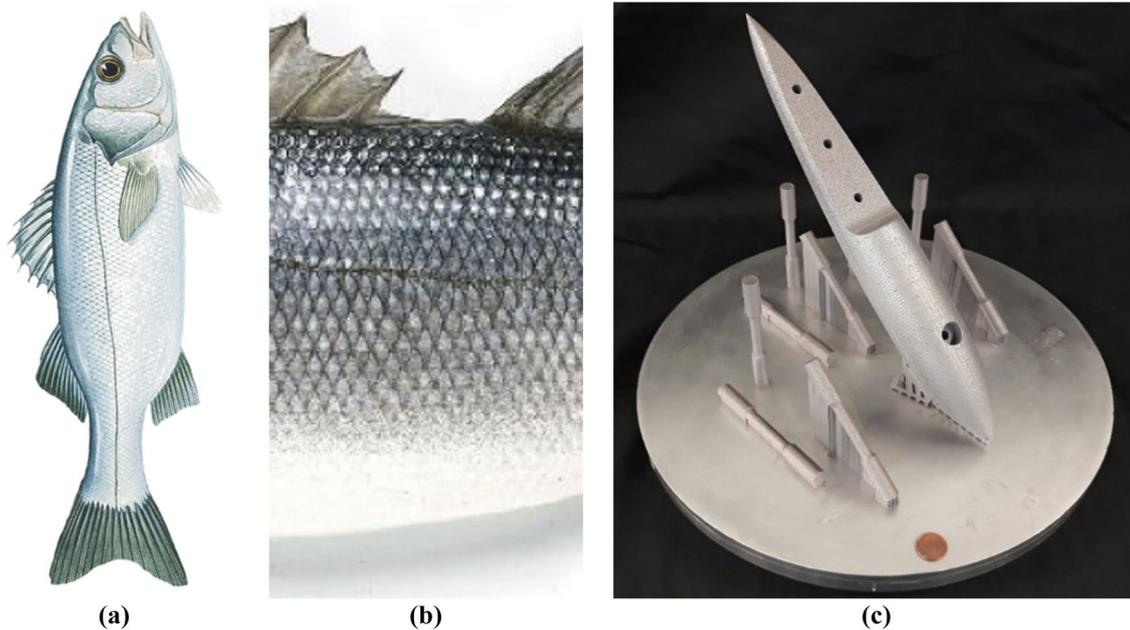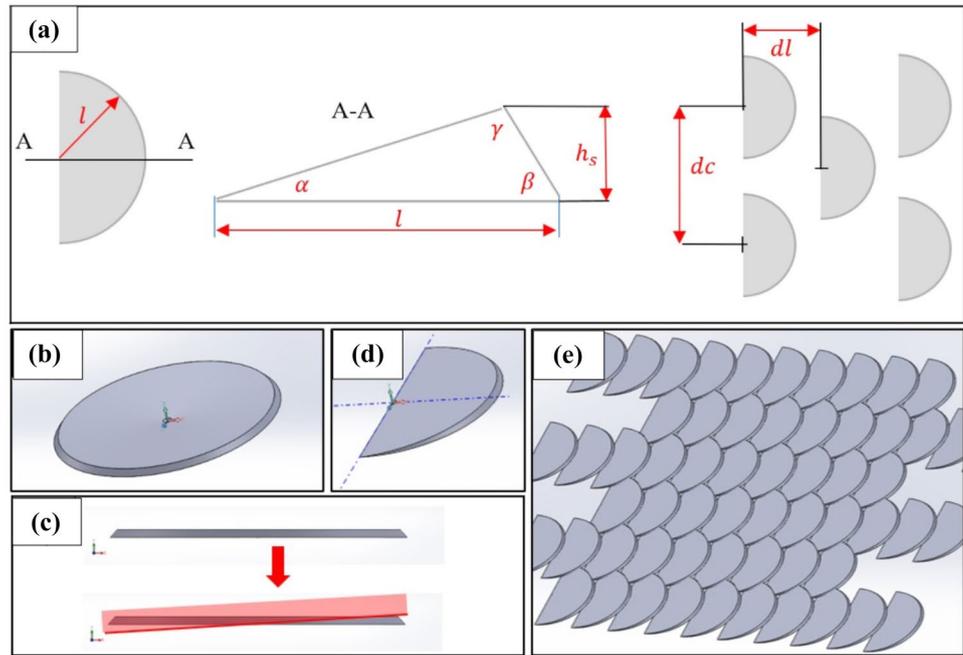

Fig. 1 Scale geometry and pattern design; **a** parametrization, **b** revolution solid, **c** cut, **d** final scale, **e** reference reproduced pattern example

Fig. 2 Domain **a** upper view, **b** detail on scales equipped zone, **c** perspective and boundary conditions, **d**) single scale, and **e**) scale pattern

Table 1 Scale design parameters used in the additive manufacturing and CFD study

Fixed parameter		Level
β (deg)		47
Varied parameters	Low	High
α (deg)	3.0	4.5
l (mm)	2.00	3.00
dl (mm)	0.90	1.35
dc (mm)	6.00	9.00

this first study, rather than focusing on smaller geometries. The aim was to generate data that may be compared to future experimental tests.

By increasing the scale radius, the interaction of one scale with the others increases and so dl and dc come into play. To obtain an acceptable bio-mimicking scale pattern, it was necessary to increase the scale distances to compensate the superimposition. The chosen high level of l was small enough to obtain an acceptable pattern result even with low levels of dl and dc. The variations of α and l resulted in a significant change in the scale geometry, maintaining similar shape with respect to the reference geometry. The midsection (Fig. 2a, section A–A) covers the four configurations reported in Appendix 1. Table 2 reports the h_s values determined by the (α, l) combination. The behaviour of each scaled pattern is compared to the one of the corresponding plate with no scales. The impact angle can be 3° or 4.5° while the cross-section has the same height of the scales (0.10, 0.15 or 0.22 mm). Four groups were generated (Table 2).

Table 2 Maximum scale height values for each combination used in the additive manufacturing and CFD study

α (deg)	l (mm)	h_s (mm)	Group
3	2	0.10	A
4.5	2	0.15	B4.5
3	3	0.15	B3
4.5	3	0.22	C

3 Additive manufacturing feasibility

Production of the textured surface requires verification of the capabilities of the employed process. The ideal surface texture is realized using suitable CAD software, prepared for the 3D printing and made using a metal alloy. The surface finishing is characterized so that the CFD analysis will be able to use the real surface roughness for the fluid dynamic

performance assessment. The capability of reproducing the scale geometry is verified for the as-built prototype and for the treatment of the surface with sandblasting to increase the smoothness of the model.

3.1 Modelling of the fish scales on free-form surfaces for LPBF feasibility

The conditions provided in Table 1 were considered in this part of the study. The software used to model the geometries were Dassault Systèmes Solidworks and Rhinoceros. Solidworks, as used to design the base model of the specimens carrying the scales as well as to develop the parametrized model of fish scale pattern, was used to apply fish scale patterns and to generate STL models to be loaded in CFD and CAM environments. Boolean union among scales is required since during the Solidworks modelling, using a linear pattern command to obtain the fish scale pattern, a multitude of detached bodies were generated. Each scale was an independent body, an aspect of great help when dealing with pattern adjustment to the chosen dimensions. The second utilization for Rhinoceros in modelling was to adapt scales to the non-planar surface of the specimens. The specimen geometry was a hollow body consisting of a cylindrical section closed with hemispherical ends. This geometry was designed to incorporate different printing orientations as well as allowing reproduction of the pattern with acceptable geometrical deformation (Fig. 3a, b). The external radius was 20 mm, while shell thickness was 1 mm, both uniform

over the entire model. The specimen was oriented with its main axis at 45° with respect to the build direction in order to emulate the most common build direction to limit thermal distortions and use support structures. A lateral tail was inserted to host specimen codes (01–16), while a powder evacuation hole was left at the bottom (Fig. 3c). Pyramidal supports were inserted to allow easy detachment, elevation and self-standing of the specimen. Internally, tree-shaped support geometry was modelled to support the overhanging portion of the upper hemisphere (critical angle 45°). The maximum distance between column upper anchors was 3 mm. All the 16 different scaled patterns were modelled and applied over a correspondent base model copy (Fig. 3d, e). The complete STL models were transferred into Materialize Magics (Fig. 3f) for platform preparation. The specimens were placed in a random order on the build platform. The specimens were orientated at 45° with respect to recoating direction and they grow in height linearly exposing up-skin portions to the recoater. Due to convergent geometry of base model (hemispherical ends), the scaled pattern is made to converge as well, imposing a gradual decrease in scale dimensions. This aspect allowed observation of the reproducibility of the scaled pattern in reduced dimensions, going toward smaller details.

3.2 LPBF system

An industrial LPBF machine (Trumpf TruPrint 3000) with ø300 mm×400 mm build volume was used to process the
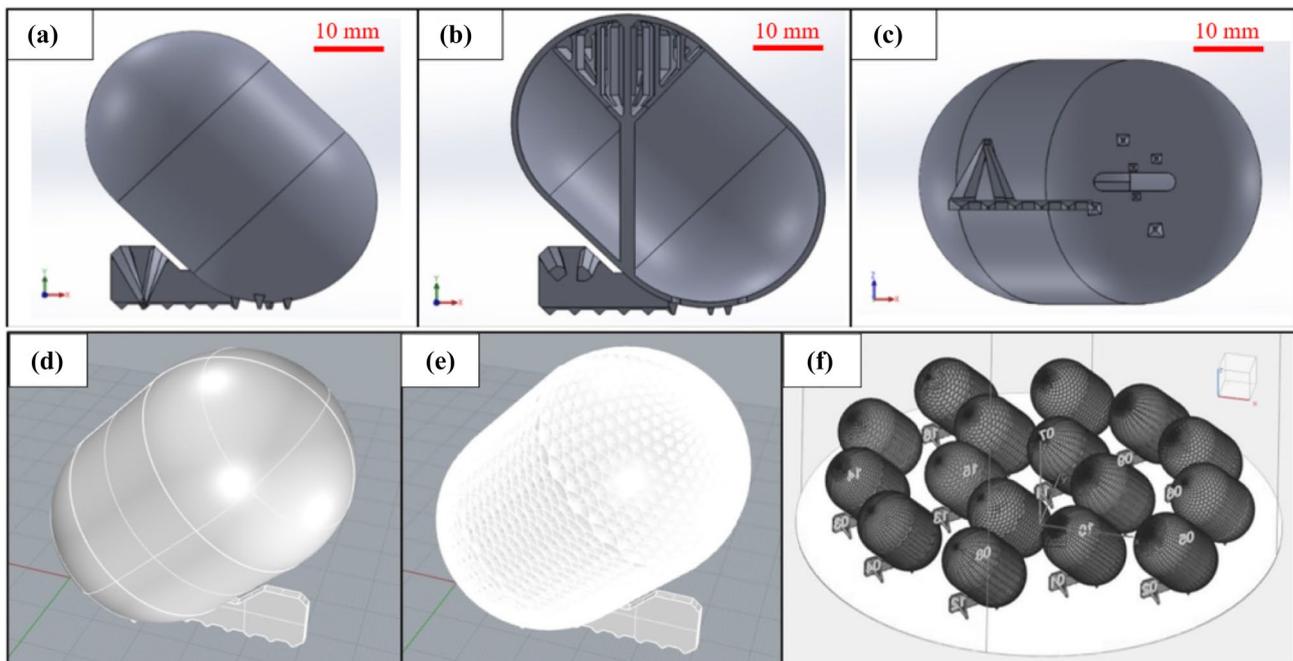
Fig. 3 Specimen base model, (**a**) exterior, (**b**) section of interior, (**c**) bottom. Scaled pattern application, (**d**) base model, (**e**) scale-equipped model specimen carrying scale code 03, (**f**) completed virtual building platform (size ø300 mm)

AlSi7Mg0.6 alloy chosen for the study. This material has been used extensively in aerospace, aviation and automotive applications due to its light weight and good processability via LPBF [27–29]. The powder used was characterized by a 20–63 μm powder grain size and produced by means of gas atomization. The process chamber was filled with Argon operating at a 1000 ppm oxygen level. The main process parameters are reported as in Table 3. On the produced specimens, a beam compensation of 0.13 mm was employed with two border scans. The LPBF built processor used Materialize Magics software to prepare the building platform in the digital environment.

3.3 Characterization of the surface texture

The geometrical fidelity of the bio-mimicking surface produced was evaluated through focus variation microscopy (Alicona Infinite Focus). Surface height maps were acquired with vertical and lateral resolutions, respectively, at 1 μm and 15 μm. The acquisitions were followed by a form removal procedure tool together with a coordinate system adjustment, to centre the dataset over the origin of the reference system. To distinguish between surface roughness elements and fish scale geometrical features, a cut-off wavelength of 0.8 mm (ISO4287) was used for all roughness measurements. This value was smaller than the minimum periodicity length imposed by scale pattern geometries. Sandblasting was used on the produced surfaces to assess eventual benefit on surface quality and scale geometry reproduction (Guyson F1600 Blast System). The pieces produced were sandblasted with an inclination of about 45° with respect to the vertical jet.

Each specimen was acquired via focus variation microscopy. Primary profile analysis was used to compare the surface profile produced with the theoretical dimensions. For the roughness measurements, paths of 10–15 mm were selected to comply with the cut-off wavelength. Three paths were selected (Fig. 4a) to measure average roughness (R_a).

Table 3 Overall volume LPBF process parameters involved

Process parameter	Level
Chamber oxygen concentration (%)	0.1
Inert gas type (–)	Ar
Shielding gas flow rate (m/s)	0.8
Preheating temperature (°C)	100
Laser spot diameter, d_s (μm)	100
Layer thickness, z (μm)	50
Layer scan strategy (–)	No pattern
Scan direction rotation (°)	67
Laser power, P (W)	345
Scan speed, v (mm/s)	1500
Hatch distance, h (mm)	0.10

Primary profile analysis was performed choosing three profiles lying on the mid-planes of the scale rows (Fig. 4b). For each primary profile, the mean peak to valley distance (Δpv_{meas}) as collected (Fig. 4c). This distance was used to generate a prior assessment of quality, comparing with the theoretical distance imposed by the 3D original model, namely Δpv_{theo} (Fig. 4d). To compare different scale pattern results, the absolute geometrical error, with respect to the correspondent reference geometry was computed as:

$$\Delta(\Delta pv) = \Delta pv_{meas} - \Delta pv_{theo}. \tag{1}$$

Two different zones of the as-built specimens were analysed, namely Zone1 and Zone2 as shown in Fig. 5. Zone1 was chosen to study the pattern in a semi-planar or slightly curved condition and its reproducibility with respect to theoretical dimensions. Zone 2 was chosen to observe scale quality when dealing with progressively smaller dimensions as the scale pattern converges. The areas analysed contained down-skin, vertical and up-skin portions due to the printing orientation of the specimens. In the MeshLab environment, acquired 3D datasets were loaded, together with their correspondent specimen theoretical STL file. For one dataset at time, alignment and Hausdorff distance were computed. Mean distance was stored as a response. Zone 1 3D datasets were used for primary profiles, roughness analysis as well as mean distance. Zone 2 analysis was limited to the theoretical geometry comparison. Analysis of variance (ANOVA) was carried out with a significance level of 0.05 on the response variables.

4 CFD model and computational domain setup

The CFD model realized allows us to consider the fluid dynamic performance of the scale-equipped surface, considering not only the scale geometry, but also the surface finishing, in terms of equivalent roughness. The study is not performed on the rudder bulb geometry, but on a flat plate equipped with the scales, to reduce the computational cost.

4.1 Numerical setup

The domain is inspired by the one used by Muthuramalingam et al. [11] A single full scale row with neighbouring row halves is inserted, using periodicity (i.e. cyclic condition) on the lateral faces, thus emulating the existence of the pattern, but avoiding lateral end effects (Fig. 6). This domain had a scale-equipped portion of 50 mm by 6 mm in the XY plane. The flow is directed as the X direction and the Y dimension were equal to the transversal spacing (dc) of
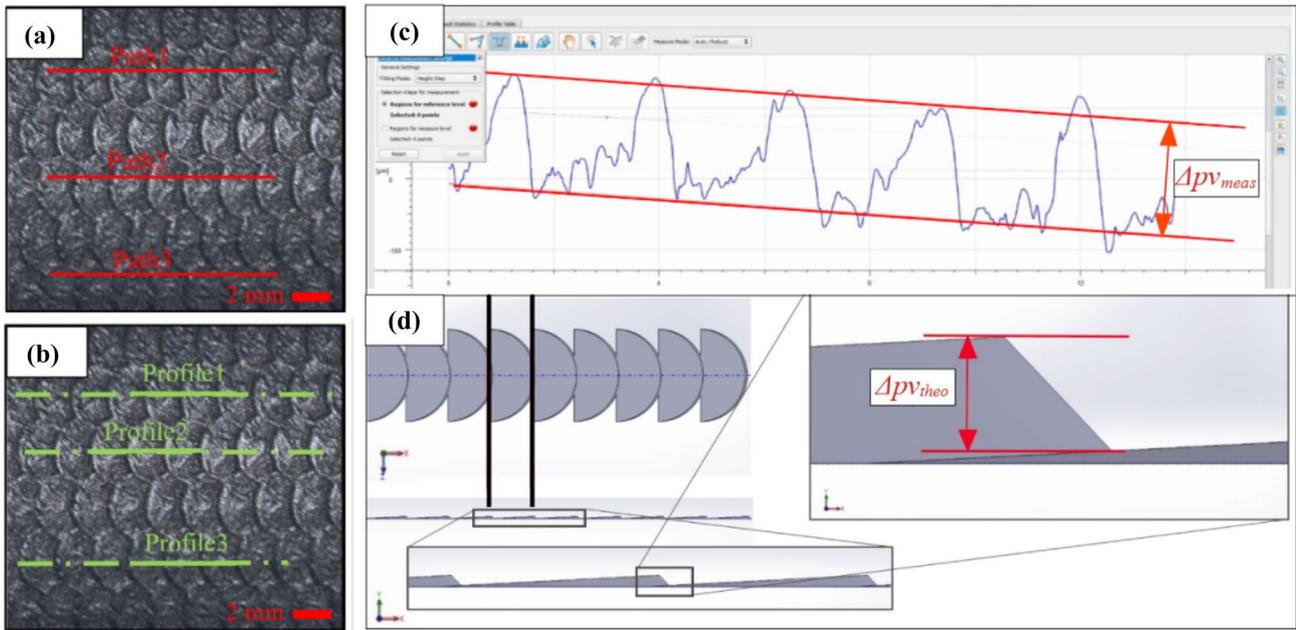
Fig. 4 (**a**) Example of the roughness measurement paths, (**b**) primary profile example, (**c**) measured mean peak to valley distance (**d**) theoretical peak to valley distance from scale pattern CAD model

Fig. 5 Areas analysed, general view and example of obtained 3D data sets

the scales, allowing the obtained model to be consistent in terms of lateral spatial repetition to form a pattern. A no-slip boundary condition was applied on the surface of the scales.

The liquid considered was water (Newtonian and incompressible) with density (ρ) of 10^3 kg m^{-3} and kinematic viscosity of 10^{-6} s m^{-2}. Incompressible Reynolds-Averaged Navier–Stokes (RANS) equations were solved within the OpenFOAM framework to reproduce the flow over the scales, to observe particular flow features (such as streaks [11]). The incoming fluid speed was fixed at the inlet (1.25, 2.5, 5 m/s), while a pressure equal to 0 (incompressible flow) was prescribed at the outlet. A null velocity gradient is determined at the outlet and for pressure at the inlet. The k–ω SST turbulence model proposed by Menter et al. is chosen [26]. To define the boundary conditions for turbulent kinetic energy (k) and turbulent dissipation rate (ω), the turbulence intensity was set as 1% and the reference length as the longitudinal length of the test plate. Convergence of the results was verified monitoring the residuals, as well as the forces on the scales and the velocity at some points.

The main interest was to calculate the force components parallel to the main flow direction that constitute the drag force. The drag force (F_d) can be divided into the contribution of pressure and viscous force components in X-direction, F_{p_x} and F_{v_x}, called F_p and F_v in the following for simplicity:

$$F_d = F_p + F_v. \tag{2}$$

The drag force coefficient C_d and the viscous force component coefficient C_v were obtained by considering the total projected frontal area "impacting" the stream orthogonally, A_{front}:

$$C_d = F_d (0.5\rho U_\infty^2 A_{front})^{-1}, \tag{3}$$

Fig. 6 Domain (**a**) upper view, (**b**) detail on scale equipped zone, (**c**) perspective and boundary conditions
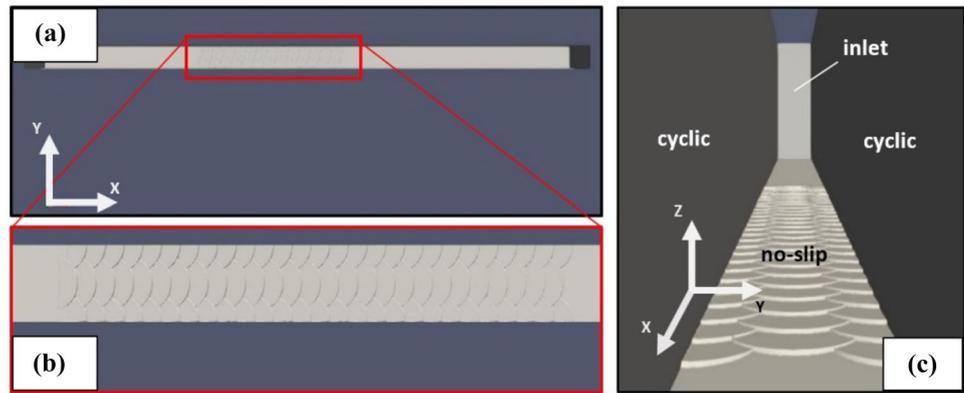
$$C_v = F_v (0.5 \rho U_\infty^2 A_{\text{front}})^{-1}, \tag{4}$$

where U_∞ is the main stream velocity and ρ the fluid density. To compare drag entities related to different geometries, their values were observed versus the drag forces generated by a correspondent scale-unequipped plate, designed to have the same frontal area, scale angle α (as frontal impact angle) and longitudinal length. Coefficient variations were determined as in the following (Y stands for presence of scales, N stands for no scales):

$$\Delta C_d = (C_{d, Y} - C_{d, N}) C_{d, N}^{-1}, \tag{5}$$

$$\Delta C_v = (C_{v, Y} - C_{v, N}) C_{v, N}^{-1}. \tag{6}$$

A mesh independency study was conducted, to guarantee reliable results. The results reached convergence around 11 million cells; in Fig. 7 results are normalized with respect to the ones of the selected discretization. The domain (Fig. 8) consists of approximately 96% hexahedral cells, 3.6% polyhedral and less than 1% in prisms.

4.2 Effect of scale design and surface roughness on water drag

In the initial part of the work, the scales designed were assessed via CFD using the STL without any surface curvature or roughness and under the experimental conditions reported in Table 1. Collected responses were F_p, F_v, F_d, C_v and C_d as well as the differences ΔC_v and ΔC_d, between the scale-equipped and plain models.

A sensitivity analysis with different fluid speeds and surface roughness was then done employing the flat field. The reproduction of surface roughness is defined through an equivalent sand grain diameter (k_s) [30–33]. The scale-equipped plate with most promising results in terms of drag reduction in the first analysis was considered as the fixed scale model; in Appendix 3, the model was adopted to relate surface roughness with the sand grain diameter. Roughness
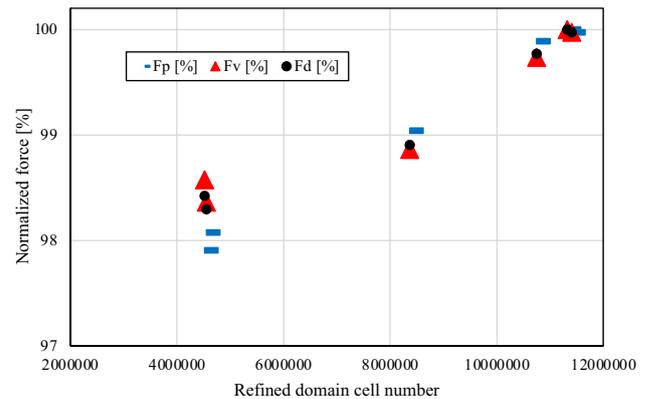
Fig. 7 Mesh validation results; data are normalized with respect to selected refinement level. Cell number referred to reference European bass scale pattern geometry

levels were measured on the LPBF produced specimens and set to represent, respectively, the smooth, polished, sandblasted and as-built conditions (Table 4).

5 Results and discussion

5.1 Geometrical errors and surface roughness of the LPBF produced specimens

Figure 9 shows the build platform with the specimens produced. The surface roughness and geometrical error values are reported in the Appendix 2 (Table 8). The measured R_a values were in a common range for LPBF as-built surfaces between 10 and 15 μm. Roughness values were considered satisfactory since they were much less than the Δpv_{theo} and Δpv_{meas}. This suggests that roughness components do not interfere substantially with scale geometry. However, to smooth local irregularities, a surface finishing may be of help. Figure 10 shows the main effects and interaction plots of the response variables. The main effects plots depict the change between the global mean values of the

output as a function of the employed parameter. The interaction plots show the relationship between one factor and a continuous response depends on the value of the second factor. Both the main effects and interaction plots are only complementary to the analysis of variance. Table 5 shows the results of ANOVA for each output considered. Considering R_a, the results show that only α has a statistically significant effect with a value close to a level of statistical significance. This weak effect suggests that the surface roughness generated by the LPBF process does not depend noticeably on the surface design parameters.

Concerning $\Delta(\Delta pv)$, α and l are significant along with the interaction between l and dl. Scale peak to valley distance is nearer to the reference model the bigger the geometry (i.e. high levels of α and l). Error increases as the geometry becomes smaller. Such errors can be expected to be due to the layering method used in the LPBF process. Indeed, the discrete layer size will result in excessive or insufficient height depending on the size of the scale pattern. The highest error levels are approximately 25 μm, which can be expected to be due to the shrinkage of the final melted layer that results in approximately half the layer thickness. The negative $\Delta(\Delta pv)$ values correspond to a profile that has peaks closer than expected. With higher α and l, it can be expected that the overall contribution of the surface roughness and irregularities may play a marked role in decreasing the distance.

Concerning the mean distance, the most relevant parameter appears to be the Zone. Zone 1 develops along several layers, while Zone 2 is the top side of the specimens


Fig. 8 Full domain, box dimensions 175 × dc × 15 mm, (**a**) lateral view; (**b**) detail on scale pattern mesh refinement, (**c**) perspective
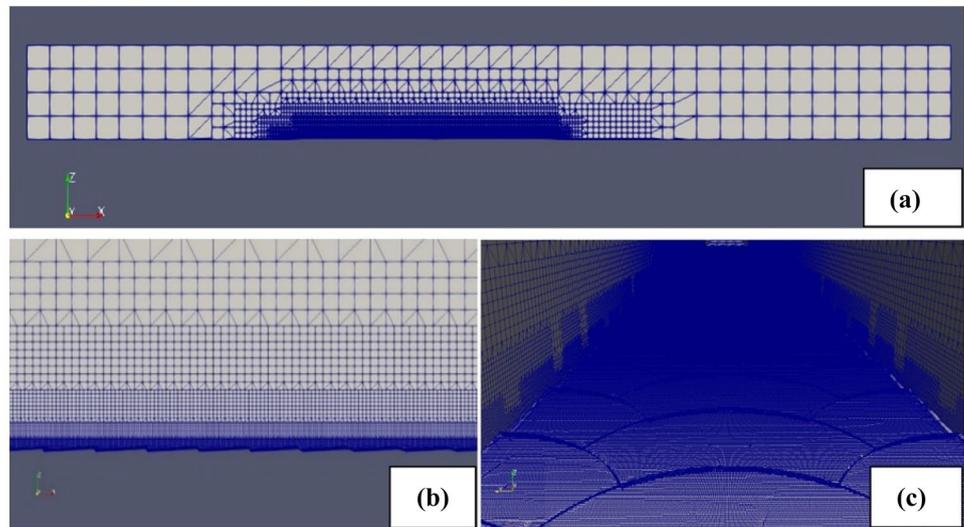
Table 4 Roughness, speed and geometry levels used in the sensitivity analysis

Factor	Levels
Equivalent sand grain diameter [k_s (μm)]	0, 3.7, 23, 70
Speed [U_∞ (ms^{-1})]	1.25, 2.50, 5.00
Geometrical model	Scale-equipped, Plain

Fig. 9 The produced surface textured samples on the build platform (**a**) side view, (**b**) back view
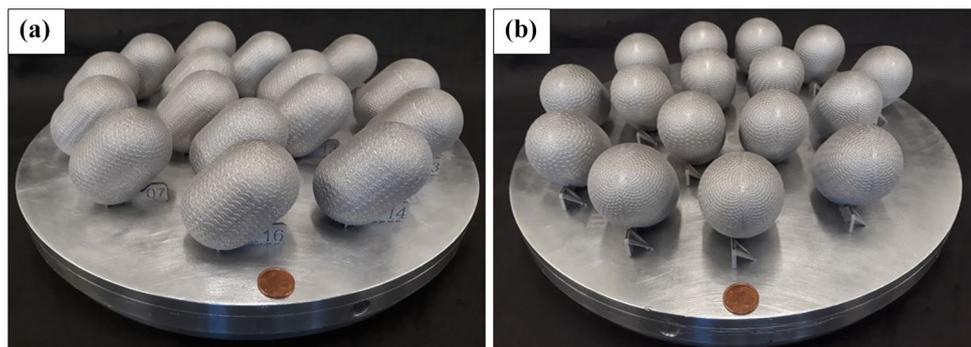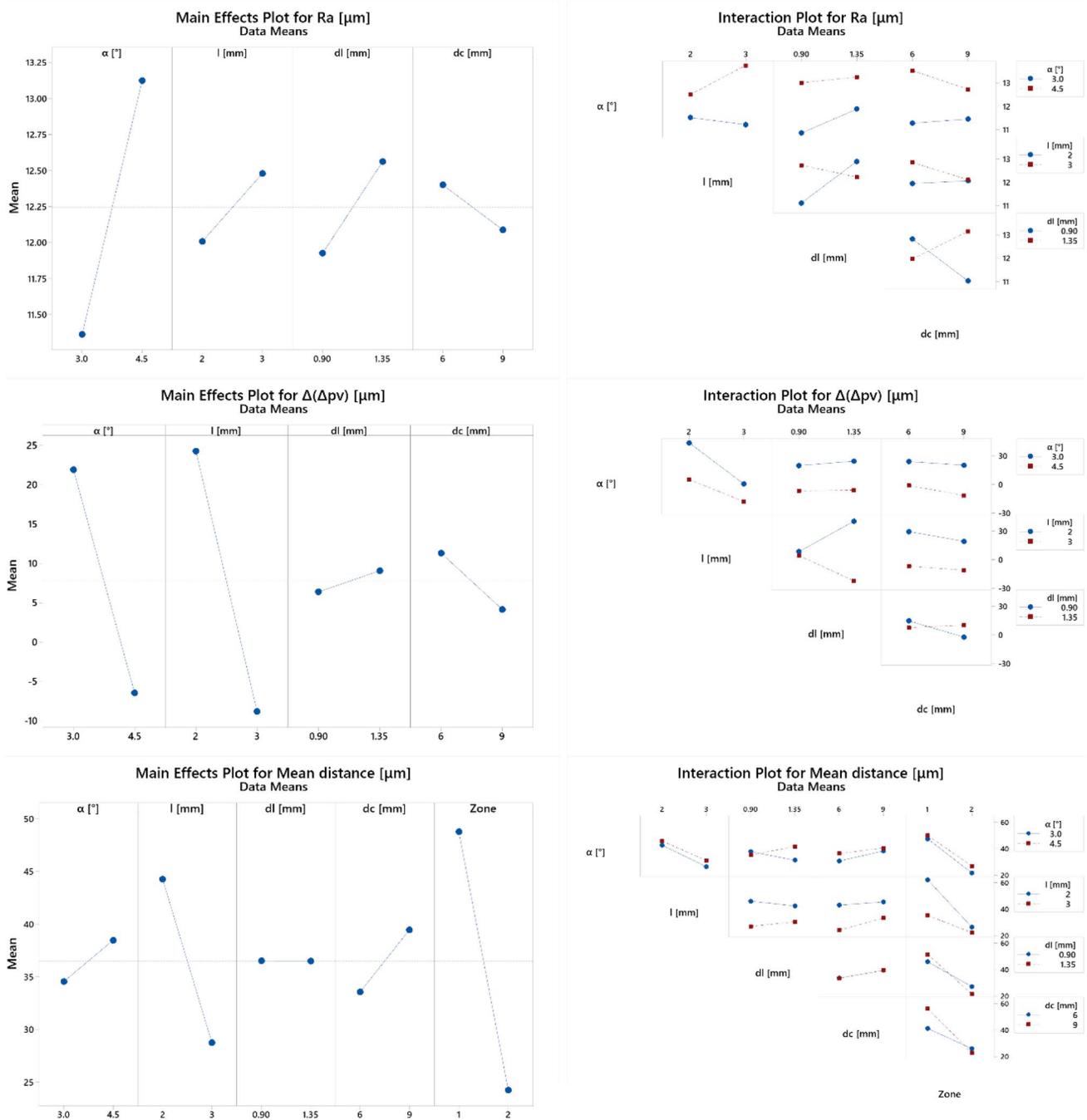
Fig. 10 Main effects and interaction plots for R_a, $\Delta(\Delta pv)$ and mean distance

resulting in a smaller number of layers to be built. Within the statistical analysis, Zone 1 is analysed as a blocking factor, hence its interactions with other parameters were not included in the analysis, but included in the interaction plot in Fig. 10. A qualitative analysis can be made on the interactions with the plotted graph only indicating a weak possibility l and *dc*. Overall, the results show that within the

manufactured curved surfaces, geometrical accuracy can vary locally due to surface roughness changes, melt pool shrinkage, discrete layering and possibly thermal deformations. Despite such issues, the very fine details involved were found to be replicable with discrete fidelity compared to the digital files.

Table 5 Simplified ANOVA tables showing p-values of the parameters for each response

Source	R_a	$\Delta(\Delta pv)$	Mean distance
α (°)	*0.044*	*0.013*	0.497
l (mm)	0.506	*0.007*	*0.013*
dl (mm)	0.379	0.733	0.999
dc (mm)	0.656	0.383	0.312
Zone	n/a	n/a	*0.000*
α (°)×l (mm)	0.292	0.236	0.890
α (°)×dl (mm)	0.583	0.805	0.265
α (°)×dc (mm)	0.494	0.666	0.770
l (mm)×dl (mm)	0.143	*0.012*	0.538
l (mm)×dc (mm)	0.546	0.714	0.559
dl (mm)×dc (mm)	0.074	0.250	0.999

Statistically significant parameters are shown in italics (n/a—not available)

Sandblasting was performed on the specimen carrying the most promising pattern (code 03). Surface quality and scale reproduction are improved with respect to the as-built condition. R_a is decreased to 6.6 μm and $\Delta(\Delta pv)$ is brought to -7.3 μm. It can be expected that the sandblasting process removes the sintered particles and smoothens the surface to a degree that both the surface roughness and peak to peak distance is reduced. Although not specifically tested other conditions, the employed sandblasting procedure is expected to remove evenly all around the specimen geometry by removing the sintered particles. However, prolonged exposure to sandblasting may indeed cause excessive erosion and the loss of the surface pattern. In the light of the CFD analyses, it can be concluded that the production cycle via LPBF and a light surface treatment such as sandblasting can produce the desired surface pattern effectively.

5.2 Effect of scale parameters on hydrodynamic drag

With a confirmed manufacturing feasibility of all the desired patterns, the investigation of the pattern dimensions on the drag reduction became more relevant. Table 6 collects the calculated forces and drag coefficients with scaled and plain surfaces. Patterns 03 and 11 show drag reduction with respect to the correspondent scale-unequipped plate (Table 6). A noticeable difference in drag generation is observable in configurations having $\alpha = 3°$ that are generally able to generate less drag than those with $\alpha = 4.5°$. Pattern 03 differs from the reference configuration (01) only by the scale radius, showing higher drag reduction. For 01, the limited drag increase obtained is considered acceptable, since parametrization, modelling and generation of pattern may not coincide with the 3D natural—scanned model adopted

by Muthuramalingam et al. [11] Scaled patterns appear sensitive to the viscous drag component. Even if higher pressure drag can be observed, probably due to consecutive impacts of the stream toward scales, the viscous contribution is lowered at a point that in many cases leads to almost null drag variation. In some cases, the variation in viscous force is larger than the variation of pressure force, generating a reduction of drag force. For ΔC_v, configuration 03 was not found to be the best in terms of viscous component reduction but the scale pattern has to deal with both the viscous and pressure components. If scales generate excessive pressure drag, the viscous advantage (i.e. shear stresses reduction) may be insufficient, as it appears to be for pattern 08, one of the patterns with a high α level.

Peculiar behaviours of the flow can be observed for scale patterns that show noticeably reduced viscous drag, coherently with the findings of Muthuramalingam et al. [11] Fluid three-dimensional trajectories (Fig. 11) appear on relatively compact scale patterns (i.e. relatively small or no gap between scales, substantial overlap of scales). This trajectory is thought to be linked to the mechanism of drag reduction, forcing a rapid action of flow separation and reattachment.

By looking at the mid positions of scales, where their height reaches h_s value (Fig. 12b), the fluid motion appears to evolve in localized vortices due to flow separation from the surface and consecutive reattachment. They are thought to behave like bearings with respect to the main flow. Different vortex dimensions are observed depending on the scale pattern. It appears that high drag generated scale patterns are characterized by elongated vortices in the main flow direction, while more compact vortices result in lower drag (e.g. pattern 03). By analysing different positions along the scale edge along the transversal direction (*Y*-direction, Fig. 12a), curved trajectories above scale superposition regions can be viewed (sections C–C, D–D and E–E, Fig. 12) as velocity direction representative vectors point inward or outward (with respect to *XZ* plane). By looking at position E–E, no relevant vortex formation was observed as steps are too small. As the scale edge is curved, also vortex axes appear to rotate, remaining tangent toward the scale profile. At curvature locations small vortices, whose axes are perpendicular to the local flow direction (i.e. tangential to the curved scale edge) can be seen. This is preserved even in the scale midsection (Fig. 12b) where, however, the main stream is perpendicular to the scale edge. The behaviour is found to be symmetric over the other half domain.

As scale patterns consist of scale rows beside each other, the fluid encounters higher and lower obstacles. This appears to generate corridors at higher and lower speeds (i.e. streaks, Fig. 13a). No evident vortex with axis is oriented in the main flow direction in any simulation. Thus, the results show corridors of different speeds that do not rotate noticeably around their own axis. In Fig. 13e, section A–A, the initial

Table 6 Results of the CFD analysis with scaled and plain plates. Force modules are referred to the test plates surfaces (50 mm × dc)

Code	Type	α (deg)	l (mm)	dl (mm)	dc (mm)	F_p (mN)	F_v (mN)	F_d (mN)	C_v (−)	C_d (−)	Group	ΔC_v (%)	ΔC_d (%)
01	Scaled	3	2	0.9	6	1.278	4.712	5.990	2.513	3.194	A_6	− 15.3	+ 3.0
02	Scaled	4.5	2	0.9	6	2.194	4.647	6.841	1.652	2.432	B4.5_6	− 17.9	+ 13.4
03	Scaled	3	3	0.9	6	1.404	4.521	5.926	1.608	2.107	B3_6	− 19.9	− 1.0
04	Scaled	4.5	3	0.9	6	2.388	4.180	6.568	1.013	1.592	C_6	− 26.1	+ 3.8
05	Scaled	3	2	1.35	6	1.429	4.847	6.276	2.585	3.347	A_6	− 12.8	+ 7.9
06	Scaled	4.5	2	1.35	6	2.554	5.109	7.663	1.817	2.724	B4.5_6	− 9.7	+ 27.0
07	Scaled	3	3	1.35	6	1.597	4.416	6.013	1.570	2.138	B3_6	− 21.8	+ 0.4
08	Scaled	4.5	3	1.35	6	2.766	4.110	6.876	0.996	1.667	C_6	− 27.4	+ 8.7
09	Scaled	3	2	0.9	9	1.249	7.525	8.775	2.676	3.120	A_9	− 9.7	+ 0.2
10	Scaled	4.5	2	0.9	9	2.251	8.260	10.510	1.958	2.491	B4.5_9	− 4.4	+ 13.1
11	Scaled	3	3	0.9	9	2.120	7.097	9.218	1.682	2.185	B3_9	− 17.6	− 0.1
12	Scaled	4.5	3	0.9	9	7.097	7.042	14.140	1.138	1.708	C_9	− 20.0	+ 42.2
13	Scaled	3	2	1.35	9	1.350	7.553	8.903	2.686	3.166	A_9	− 9.3	+ 1.7
14	Scaled	4.5	2	1.35	9	2.381	8.312	10.693	1.970	2.535	B4.5_9	− 3.8	+ 15.1
15	Scaled	3	3	1.35	9	2.450	6.898	9.348	1.635	2.216	B3_9	− 19.9	+ 1.3
16	Scaled	4.5	3	1.35	9	4.305	7.274	11.579	1.176	1.871	C_9	− 17.3	+ 16.4
A_6	Plain	3	n/a			0.253	5.561	5.815	2.966	3.101	n/a		
B4.5_6	Plain	4.5	n/a			0.372	5.661	6.033	2.013	2.144	n/a		
B3_6	Plain	3	n/a			0.342	5.646	5.988	2.007	2.129	n/a		
C_6	Plain	4.5	n/a			0.668	5.660	6.327	1.372	1.534	n/a		
A_9	Plain	3	n/a			0.425	8.330	8.754	2.962	3.113	n/a		
B4.5_9	Plain	4.5	n/a			0.654	8.639	9.293	2.048	2.203	n/a		
B3_9	Plain	3	n/a			0.608	8.616	9.224	2.042	2.186	n/a		
C_9	Plain	4.5	n/a			1.146	8.798	9.945	1.422	1.607	n/a		

Fig. 11 Periodically curved flow motion; in red, flow lines oriented as the local speed of the fluid (scale pattern 07)
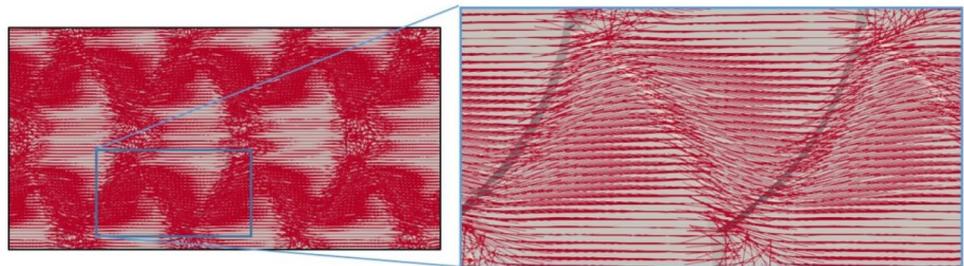
formation of streaks can be seen. A weakly visible feature is the lateral sides which start to decrease in speed, as also seen in the centre line of the domain. In B–B and C–C, it is possible to observe an evident alternation of lower and faster portions above the scales. Such zones represent streams of fluid moving at different speeds. The phenomenon appears to grow, as the boundary layer does, involving higher portions (D–D and E–E). It is particularly interesting to notice that the zones corresponding to fluid at higher speed are where the scales are superimposed. It appears that the curved trajectories are closely linked to this phenomenon, while slower portions appear to be above greater vortex portions.

5.3 Effect of surface roughness on water drag

The LPBF produced specimens revealed that surface roughness is relatively high and definitely not negligible. Hence, the inclusion of surface roughness becomes of greater importance for a better understanding of the surface pattern. Including the surface roughness a slight reduction in drag is obtained at all speed levels. From Table 7, it appears that a scale-equipped surface leads to slightly lower drag generation. In all the results, no significant difference can be observed in the roughness levels representing polished and sandblasted conditions. As speed increases, the pressure drag shows a growing disadvantage in having a scale-equipped surface. However, at low speeds, the difference is limited.
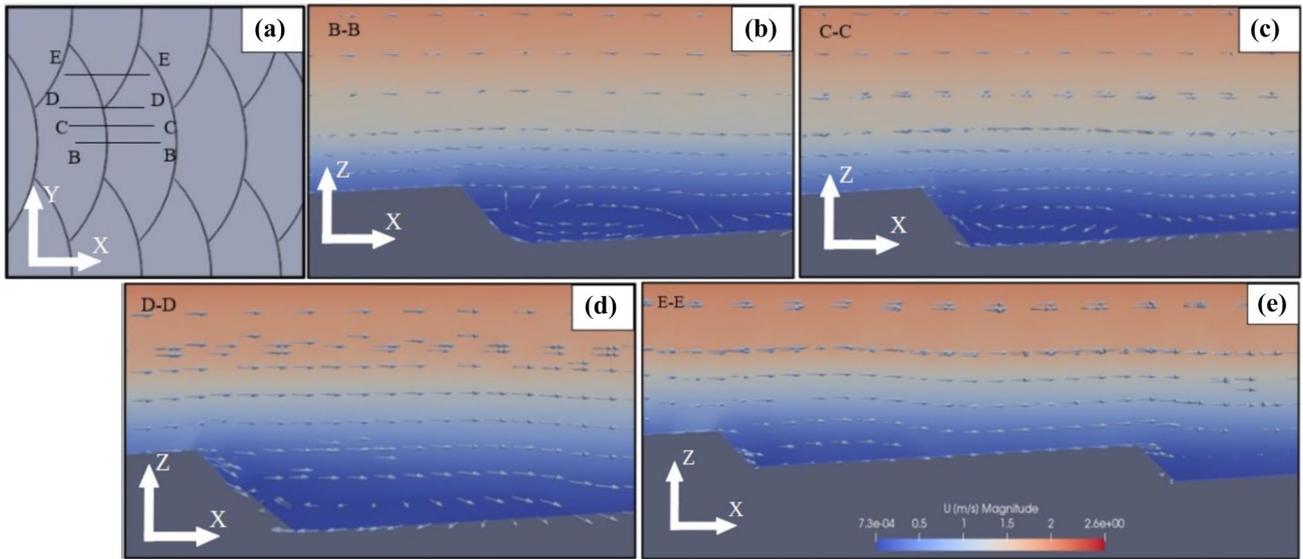
Fig. 12 Vortices on different Y-wise positioned sections, scales reproduced here are of pattern 03; (**a**) overview, (**b**) midsection, (**c**) transitional section, (**d**) complete superimposition, (**e**) partial superimposition; arrows represent fluid velocity direction
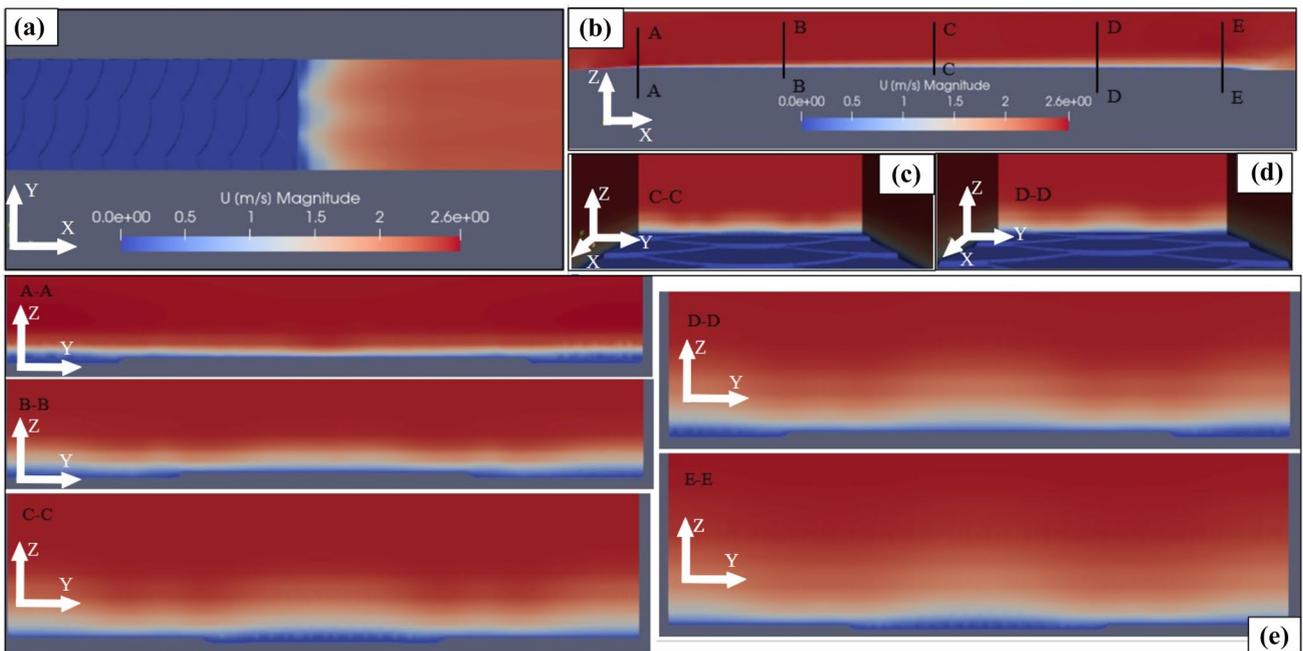
Fig. 13 Streak formation on pattern 03, (**a**) streak shape on velocity field at back, (**b**) lateral overview, (**c**) perspective on C-C section, (**d**) perspective on D-D section, (**e**) sections

Considering the viscous component of drag, the presence of roughness appears to be advantageous as the shear stresses decrease at all speeds and roughness conditions (Fig. 14a). The effect on total drag is noticeable but appears small. Drag force reduction reaches 2% for high-speed cases. A reduction is obtained in drag force at all speeds and for all surface finishes except for the smooth case at low speed. The benefit is determined by the larger effect of scales on viscous force compared to the effect on pressure. Sandblasted and polished conditions end with the same behaviour as it appears that the results do not differ noticeably by setting k_s to 23 μm or 3.7 μm. Sandblasted or polished conditions appear to improve the $|\Delta C_d|$ equally at low water speed compared to a flat surface (Fig. 14b). Sandblasting is the surface finish that

Table 7 Effect of surface roughness and the speed on the drag behaviour (force modules are referred to the test plate surface, 50 mm×6 mm)

Geometry	k_s (μm)	U_∞ (ms^{-1})	C_v (–)	C_d (–)
Most promising scaled pattern (code 03)	0	1.25	2.200	2.644
	0	2.5	1.608	2.107
	0	5	1.325	1.906
	3.7	1.25	2.345	2.737
	3.7	2.5	1.708	2.195
	3.7	5	1.496	2.051
	23	1.25	2.345	2.737
	23	2.5	1.708	2.195
	23	5	1.496	2.051
	70	1.25	2.346	2.738
	70	2.5	1.708	2.195
	70	5	1.497	2.052
Plain equivalent plate (B3_6)	0	1.25	2.430	2.554
	0	2.5	2.007	2.129
	0	5	1.800	1.929
	3.7	1.25	2.629	2.749
	3.7	2.5	2.100	2.217
	3.7	5	1.970	2.094
	23	1.25	2.629	2.749
	23	2.5	2.100	2.217
	23	5	1.970	2.094
	70	1.25	2.629	2.749
	70	2.5	2.100	2.217
	70	5	1.970	2.094

is easily obtained on a complex surface, hence it can be conveniently chosen to enhance surface quality with respect to the as-built condition. Roughness appears to play an important role at low speed, as a drag increase of about 3.5% was obtained at 1.25 m s^{-1}, while under the same condition, a roughness accounting model still gives a small advantage (drag reduction of about 0.5%).

European bass scales may be considered as distributed roughness elements [11] over a smooth surface as well. The roughness Reynolds number can be calculated as

$$R_R = \rho U h_s / \mu, \tag{7}$$

where U is the undisturbed velocity at the maximum roughness height and μ the water dynamic viscosity. U can be set to U. (2.5 m s^{-1}) while maximum roughness height determined as h_s. R_R is considered to determine whether a possible transition from laminar to turbulent boundary layer may be expected due to geometrical characteristics. The critical R_R to induce bypass transition is given to be around 250. Muthuramalingam et al. [11] tested scales at lower speed with respect to the one selected here, therefore, their roughness Reynolds number is below the critical value. This study (2.5 m s^{-1}) leads to larger R_R (250, 375 and 550, respectively for 0.10, 0.15 and 0.22 scale height values), so transition to turbulent flow may be expected in simulation results. The event of transition, however, may be influenced also by the length of the scaled plate involved. Therefore, by having chosen a 50 mm length for comparison purposes with Muthuramalingam et al. results, may not be enough to generate transition at this speed. The maximum fluid-facing slope of the scale is 4.5° (0.079 rad). Muthuramalingam et al. reported that, from referenced studies, if the slope of

Fig. 14 Coefficient variations between scale-equipped and unequipped models
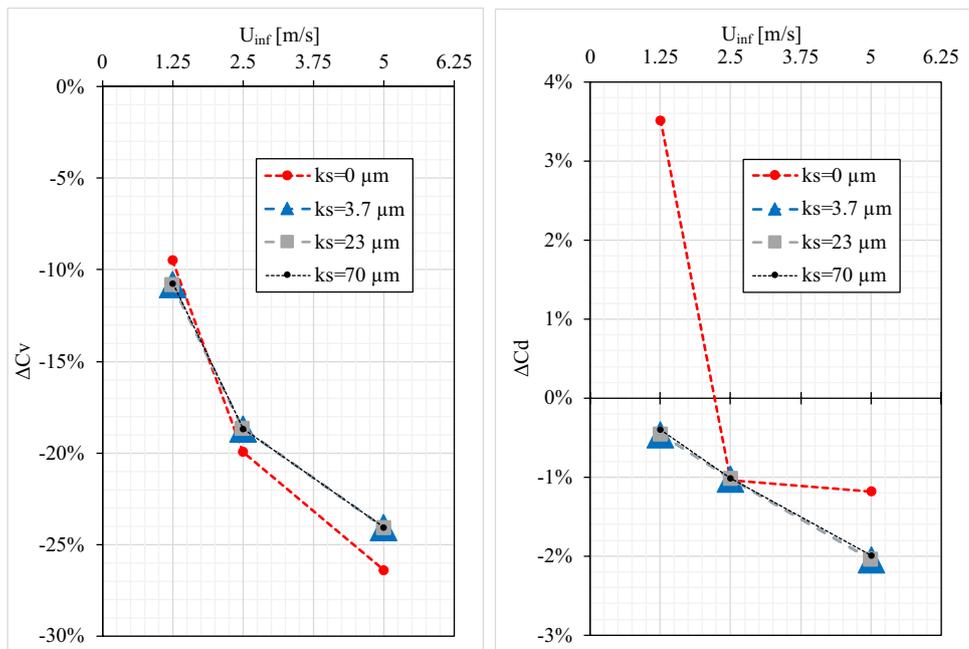
the roughness element is much less than a radiant unit (i.e. $\alpha \ll 1$ rad) then the stability of the velocity profiles (e.g. streaks formations) is increased because of the roughness. The consideration of scales as roughness elements may not be representative of a real case study where the roughness profile generated depends on the production process that superimposes it over scale geometries.

The results overall show the possibility of reducing water drag by means of opportunely designed bio-mimetic surface textures. The influence of the surface roughness, which is a smaller scale component of surface topology, is also underlined. Hence, the overall additive manufacturing cycle along with the finishing operations play an important role on the final functioning of the component. The experimental analysis regarding the performance of the designed surfaces requires further attention. A dedicated system able to reveal both the fluid flow and forces acting on the component would be required. As a matter of fact computational studies such as the one provided in this work help better discriminate along the possible solutions prior to the lengthy experimental validations. Indeed, the design and use of such experimental system will be part of future works.

6 Conclusions

In this study, a bio-inspired surface is modelled and parametrized to reduce water drag on nautical metallic components. The work assessed the surface performance via CFD, while the processing issues were analysed using LPBF and AlSi7Mg0.6 alloy. The following points can be deduced as the final conclusions.

- The designed surfaces were applied to a curved test geometry to assess the feasibility of producing the desired surface texture with the LPBF process. The results showed that the surface texture parameters did not have any noticeable effect on the surface roughness, while the geometrical errors were related largely to the position of the scale on the curved surface in as-built condition.
- The use of sandblasting was found to be sufficient to reduce the surface roughness and the geometrical errors thus confirming the feasibility of the assessed manufacturing cycle.

- The scale angle α appears to be significant in drag generation, being beneficial in its lower level (3°). The main influence of the scales is a strong reduction in the viscous drag component, while the pressure force is enhanced due to scale geometry. However, the benefit in viscous force is revealed to be great enough to balance or overcome in many cases the increasing pressure force over the surface.
- The most promising scale pattern reaches a reduction of overall drag force of about 1% at 2.5 m s^{-1} compared to its correspondent plain counterpart. The CFD analysis showed a peculiar phenomenon related to viscous drag reduction thanks to the presence of the scale pattern.
- The CFD analysis also assessed the influence of surface roughness considering the surface profiles obtainable by the LPBF process. The presence of roughness did not show a significant difference between polished and sandblasted conditions. This suggests that heavy finishing operations may not be required.

With this work, the concept of using bio-mimicking surface designs applied to metallic components has been confirmed. Indeed, experimental confirmation of the drag behaviour is required to be further implemented. The use of topological optimization for surface design is another aspect that future works should cover. The present work decoupled the scale geometry from the non-planar surface geometry of the rudder bulb intentionally. As part of this initial work, the impact of scale geometry was assessed parametrically through conditions that are faster to simulate. Indeed, the added surface curvature can change the final results locally. Future works can consider the allocation of optimal scales around the non-planar geometry for the purpose.

Appendix 1: Scale mid-section configurations, texture and unequipped plate examples

In Fig. 15 parametric modeling of a single scale is shown. In Fig. 16 an example of pattern obtained with $l = 3$ mm, $dl = 0.9$ mm and $dc = 6$ mm is shown. In Fig. 17 is shown a B4.5 scales-unequipped model as example.
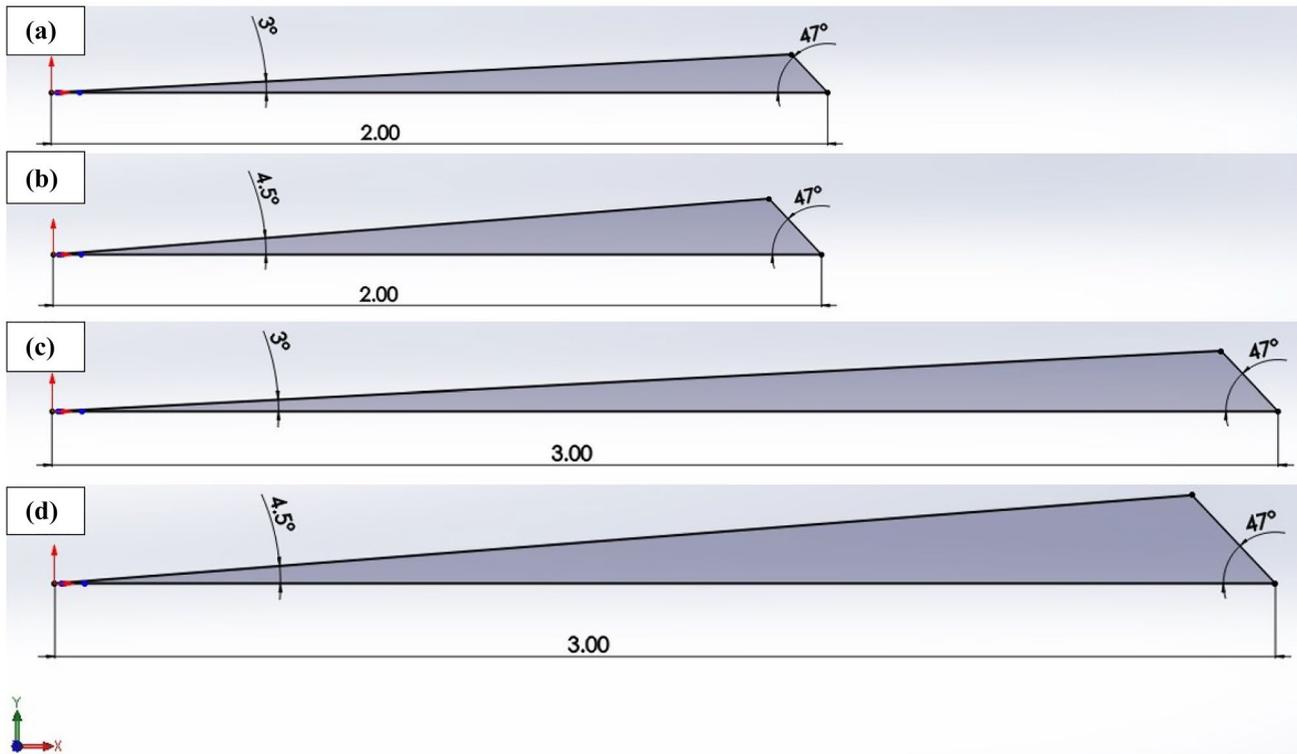
Fig. 15 Scale midsection configurations (not specified dimensions are in millimetres); **a** $\alpha=3°$, $l=2$ mm, **b** $\alpha=4.5°$, $l=2$ mm, **c** $\alpha=3°$, $l=3$ mm, **d** $\alpha=4.5°$, $l=3$ mm

Fig. 16 a Compact pattern, upper view, **b** perspective with a highlighted scale contour
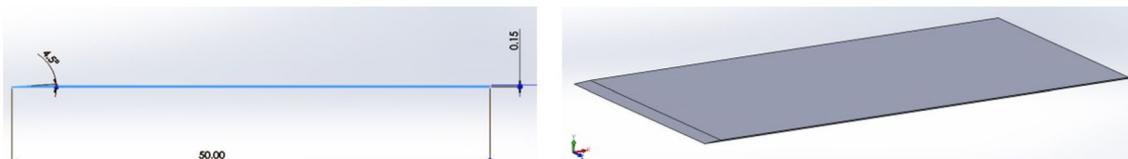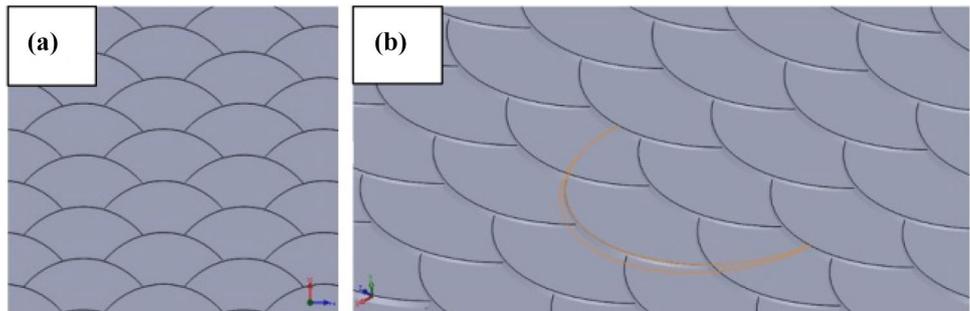
Fig. 17 B4.5 model, not specified dimensions are in millimetres

Appendix 2: Measured roughness and geometrical error data

See Table 8.

Table 8 Roughness and geometrical error responses

Pattern (–)	R_a (µm)	Δpv_{theo} (µm)	Δpv_{meas} (µm)	$\Delta(\Delta pv)$ (µm)	Zone 1 mean distance (µm)	Zone 2 mean distance (µm)
01	11.2	89.94	131.7	41.7	60.3	33.3
02	13.1	132.0	132.5	0.48	35.6	41.8
03	12.7	89.94	106.3	16.3	16.5	16.7
04	14.3	132.0	132.9	0.89	35.4	29.0
05	11.0	100.0	148.1	48.1	50.2	23.8
06	12.5	150.0	177.0	27.0	73.5	25.6
07	10.2	134.9	123.9	– 11.0	29.8	15.5
08	14.2	198.0	165.1	– 32.9	28.4	21.7
09	9.86	89.94	114.4	24.5	97.2	16.6
10	10.3	132.0	98.88	– 33.1	59.8	23.8
11	9.64	89.94	85.77	– 4.17	33.1	28.7
12	14.3	132.0	136.5	4.49	29.7	26.7
13	14.0	100.0	159.7	59.7	38.3	21.9
14	14.1	150.0	175.9	25.9	82.7	23.9
15	12.3	134.9	135.1	0.14	54.5	16.3
16	12.2	198.0	153.8	– 44.2	55.4	22.6

Appendix 3: Equivalent sand grain diameter

A relation between the equivalent sand grain diameter and the average roughness is needed to link average roughness (R_a) values to k_s by having the latter inserted in the simulations. Models are already present in literature [30–32] but here the aim of the proposed model is to approximate a relation between R_a and k_s, considering single sand grain geometry and disposition. The starting assumptions are as follows:

(a) Grains are 2D modelled and considered of 3 different shapes, equilateral triangle, square and circle;
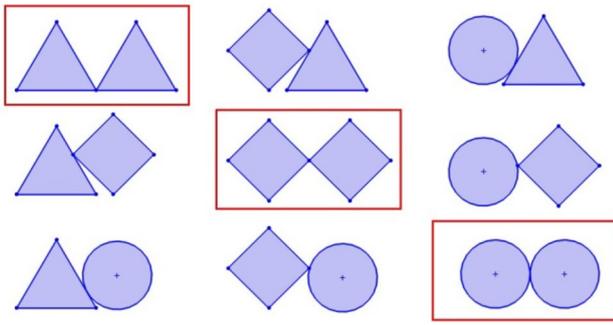(b) The surface consists of contact grains with no empty place left;
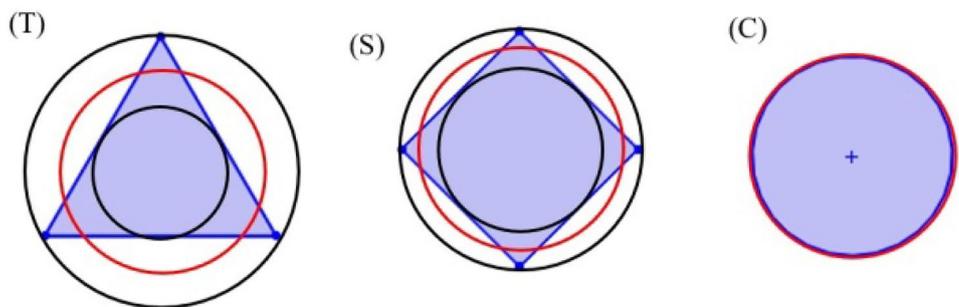
(c) Contact between grains can be of 9 types (Fig. 19);
(d) k_s is considered equal to 2 times the mean radius r_{mean} of the mean of the inscribed and circumscribed circumferences, respectively r_{insc} and r_{circ} (Eq. (8)), for each shape (Fig. 18). For the circle, inscribed, mean and circumscribed circumferences coincide with each other.

$$r_{mean} = 0.5 \times \left(r_{insc} + r_{circ} \right) \tag{8}$$

(e) All the grains have the same r_{mean} and therefore also k_s, as if they had been sieved to reproduce a certain R_a (as done experimentally by Nikuradse [33].

Assumption a) limits the grain shapes to three characteristic types to avoid intermediate cases. It has been observed that regular polygons, with number of sides between the square and the circle (6 sides and above), are not substantially distant from the results in the circle case, while a pentagon is similar to the square behaviour. Assumption b) eliminates the presence of empty spaces on the reproduced profile, however, a correction can be made increasing the presence (weight in Eq. (11)) of triangle shaped grains in contact, so as to emulate a higher presence of deep valleys. In fact, as assumption c) expresses the considered contact types among grains (limiting the analysis to the most relevant, as an upside down version of the triangle could be excluded because of less probability of appearing and lower impact on roughness), the selected three are the most relevant in terms of valley depth generated. Those combinations (red-highlighted in Fig. 19) generate the most characteristic depths of valley useful to characterize the simplified behaviour of the model. The triangles combination represents the high slope—high valley depth case, the squares are intermediate while the circles stand for small slope—small valley depth case.

Now, the strategy is to relate the r_{mean} to R_a. To do so, the general followed approach is to evaluate R_t (Fig. 20) on each combination as the maximum depth of valley (as it is done for turning method) by relating it to the specific shape side length for triangle and square cases (i.e. l_T and l_S). Then, it is possible to relate each side to the r_{mean} that is supposed to be the same for all grains. Finally, having $r_{mean} = 0.5 \times k_s$, the final relation for each case can be obtained.

Fig. 18 r_{mean} circle (red) on the three grain types, in black r_{insc} and r_{circ} circles; the three grains have the same r_{mean} and so mean diameter (k_s) as stated in assumption e); T equilateral triangle, S square, C circle

Fig. 19 Contact cases among sand grains; all grains represented have the same mean radius as they had sustained the same sieving procedure, assumption e)

The relation between r_{mean}, r_{insc} and r_{circ} is given by Eq. (7), where:

- for equilateral triangles, $r_{insc} = (2\sqrt{3})^{-1}l_T$ and $r_{circ} = 2r_{insc} = (\sqrt{3})^{-1}l_T$ that lead to $r_{mean} = (0.25\sqrt{3})l_T$;
- for squares $r_{insc} = 0.5 \times l_S$ and $r_{circ} = (\sqrt{2})^{-1}l_S$ that lead to $r_{mean} = 0.25 \times (1+\sqrt{2})l_S$;
- for circles $r_{insc} = r_{mean} = r_{circ}$.

In sequence, respectively for triangles, squares and circles configurations, relations between k_s and R_a are as in Eqs. (8), (9) and (10). The starting relation between R_a and R_t is taken as $R_a = 0.25 \times R_t$ for squares and circles while it is corrected for triangles for better representation of the geometry as $R_a = 0.5 \times R_t$.

For triangles:
$$\begin{aligned} R_a = 0.5\, R_{t,\,T} &= 0.5\left(l_T \sin 60°\right) \\ &= (0.25\sqrt{3})l_T = r_{mean} \text{ then } R_a = r_{mean} \\ &= 0.5k_s \text{ then } k_s = 2R_a. \end{aligned}$$
(9)

For squares:
$$\begin{aligned} R_a = 0.25R_{t,\,S} &= 0.25(l_S \sin 45°) \\ &= (0.125\sqrt{2})l_S = (0.125\sqrt{2})(1+\sqrt{2})^{-1}4r_{mean} \text{ then } R_a \\ &= (2+\sqrt{2})^{-1}r_{mean} \cong 0.146k_s \text{ then } k_s \cong 6.83R_a. \end{aligned}$$
(10)

For circles:
$$\begin{aligned} R_a = 0.25R_{t,\,C} &= 0.25r_{mean} \\ &= 0.125\,k_s \text{ then } k_s = 8R_a. \end{aligned}$$
(11)

In order to unify the above relations, a possible approach is to weight each coefficient to express the presence of one type of configuration to be greater or smaller than the others. As it is possible to express the general relation as $k_s = CR_a$,

Fig. 20 Maximum valley depth on chosen configurations' models
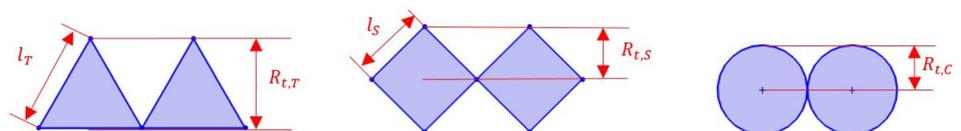
the proposed weighted equivalent sand grain diameter can be written as follows:

$$k_s = [(\textstyle\sum w_i C_i)/(\textstyle\sum w_i)] = C_w R_a.$$
(12)

As the idea is to emulate Nikuradse's sand grain [33] characteristics, an intuitive consideration is that they were not reported to be particularly round. Pursuing this objective, along with admitting eventual empty space among grains, w_i values could be adapted by having the presence of edgy grains as triangular ones to be favoured with respect to rounded type. In Table 9 proposed sets and consequent C_w values are shown.

Resulting values are of the same order of magnitude as all the models observed in literature and they have similar values with respect to the one that can be obtained from turning with a not rounded cutting tool. A noticeable difference is, however, observed with respect to turning with the rounded tool model because such a model adopts a parabolic shape for roughness profile and so a much smaller R_t value is assumed. This approximation is here considered less representative of sand grain geometries. As the study aims to manufacture the surfaces via LPBF, the considered roughness levels are related to LPBF and eventual finishing. On LPBF as-built scale-equipped surfaces as well as sandblasted surfaces, an increased presence of triangular grains with respect to circular ones would allow a better representation of the surface features because it would limit the possibility of having sand grains of dimensions unreasonably greater than scale thicknesses ($50 \div 150$ μm), by relying on a more edgy but finer emulated sand (k_s smaller). By choosing a 50%, 30% and 20% presence respectively for triangles, squares and circles (i.e. third line of Table 9), we obtain $C_w = 4.65$. In Table 10 the respective k_s values for conditions of interest are given.

The values obtained for k_s are used in the simulation software as the setting for *nutkRoughWallFunction* substituted in the *nutkWallFunction*. The *nutkRoughWallFunction* boundary condition provides a wall constraint on the turbulent viscosity, when using wall functions for rough

Table 9 Example of possible arrangements to follow the sand shape distribution

$w_{triangle}$	w_{square}	w_{circle}	C_w
0.33	0.33	0.33	5.55
0.40	0.30	0.30	5.23
0.50	0.30	0.20	4.65

Table 10 Resulting equivalent sand grain diameters for different surface roughness conditions

Condition	R_a (μm)	k_s (μm)
LPBF as-built	15	70
Sandblasted	5	23
Polished	0.8	3.7

walls, based on the turbulent kinetic energy. The condition manipulates the wall roughness parameter to account for roughness effects. This correction assumes the inclusion of any roughness profile cases, something that is not particularly realistic. However, this is considered as an acceptable approximation for the analysis as a prior approach to meet the challenge of considering roughness on numerical simulations in order to explore surface pattern behaviour when interacting with fluids.

Declarations

Conflict of interest On behalf of all authors, the corresponding author states that there is no conflict of interest.

References

1. Marine Environment Protection Committee (2008) Report of the Marine Environment Protection Committee on its fifty-eighth Session Systems (G8)
2. Liravi M, Pakzad H, Moosavi A, Nouri-Borujerdi A (2020) A comprehensive review on recent advances in superhydrophobic surfaces and their applications for drag reduction. Prog Org Coat 140:105537. https://doi.org/10.1016/j.porgcoat.2019.105537
3. Park SH, Lee I (2018) Optimization of drag reduction effect of air lubrication for a tanker model. Int J Nav Archit Ocean Eng 10:427–438. https://doi.org/10.1016/j.ijnaoe.2017.09.003
4. Pujals G, Depardon S, Cossu C (2010) Drag reduction of a 3D bluff body using coherent streamwise streaks. Exp Fluids 49:1085–1094. https://doi.org/10.1007/s00348-010-0857-5
5. Fu YF, Yuan CQ, Bai XQ (2017) Marine drag reduction of shark skin inspired riblet surfaces. Biosurf Biotribol 3:11–24. https://doi.org/10.1016/j.bsbt.2017.02.001
6. Ibrahim MD, Amran SNA, Yunos YS, Rahman MRA, Mohtar MZ, Wong LK, Zulkharnain A (2018) The study of drag reduction on ships inspired by simplified shark skin imitation. Appl Bionics Biomech. https://doi.org/10.1155/2018/7854321
7. Ran W, Zare A, Jovanović MR (2020) Model-based design of riblets for turbulent drag reduction. J Fluid Mech. https://doi.org/10.1017/jfm.2020.722
8. Song XW, Zhang MX (2019) Turbulent drag reduction characteristics of bionic nonsmooth surfaces with jets. Appl Sci. https://doi.org/10.3390/app9235070
9. Bai Q, Bai J, Meng X, Ji C, Liang Y (2016) Drag reduction characteristics and flow field analysis of textured surface. Friction 4:165–175. https://doi.org/10.1007/s40544-016-0113-y
10. Ran W, Zare A, Jovanovic MR (2019) Drag reduction in turbulent channel flow over spatially periodic surfaces. In: 2019 IEEE 58th Conf Decis Control, IEEE, 2019, pp 5918–5923. https://doi.org/10.1109/CDC40024.2019.9029688
11. Muthuramalingam M, Villemin LS, Bruecker C (2019) Streak formation in flow over biomimetic fish scale arrays. J Exp Biol. https://doi.org/10.1242/jeb.205963
12. NASA, Nasa Riblets for Stars and Stripes (n.d.) https://www.nasa.gov/centers/langley/news/factsheets/Riblets.html
13. Bechert DW, Bruse M, Hage W (2000) Experiments with three-dimensional riblets as an idealized model of shark skin. Exp Fluids 28:403–412. https://doi.org/10.1007/s003480050400
14. Dean B, Bhushan B (2010) Shark-skin surfaces for fluid-drag reduction in turbulent flow: a review. Philos Trans R Soc A Math Phys Eng Sci 368:4775–4806. https://doi.org/10.1098/rsta.2010.0201
15. Martin S, Bhushan B (2016) Modeling and optimization of shark-inspired riblet geometries for low drag applications. J Colloid Interface Sci 474:206–215. https://doi.org/10.1016/j.jcis.2016.04.019
16. An Q, Zhang B, Liu G, Yang W, Zhao H, Wang J, Wang L (2019) Directional droplet-actuation and fluid-resistance reduction performance on the bio-inspired shark-fin-like superhydrophobic surface. J Taiwan Inst Chem Eng 97:389–396. https://doi.org/10.1016/j.jtice.2019.01.015
17. Ott J, Lazalde M, Gu GX (2020) Algorithmic-driven design of shark denticle bioinspired structures for superior aerodynamic properties. Bioinspir Biomimet. https://doi.org/10.1088/1748-3190/ab5c85
18. Kogan I, Pacholak S, Licht M, Schneider JW, Brucker C, Brandt S (2015) The invisible fish: hydrodynamic constraints for predator-prey interaction in fossil fish Saurichthys compared to recent actinopterygians. Biol Open 4:1715–1726. https://doi.org/10.1242/bio.014720
19. Scarpellini A, Finazzi V, Schito P, Bionda A, Ratti A, Demir AG (2021) Laser powder bed fusion of a topology optimized and surface textured rudder bulb with lightweight and drag-reducing design. J Mar Sci Eng. https://doi.org/10.3390/jmse9091032
20. Maleki E, Bagherifard S, Bandini M, Guagliano M (2021) Surface post-treatments for metal additive manufacturing: progress, challenges, and opportunities. Addit Manuf 37:101619
21. Anilli M, Demir AG, Previtali B (2018) Additive manufacturing of laser cutting nozzles by SLM: processing, finishing and functional characterization. Rapid Prototyp J 24:562–583. https://doi.org/10.1108/RPJ-05-2017-0106
22. Senin N, Thompson A, Leach R (2018) Feature-based characterisation of signature topography in laser powder bed fusion of

metals. Meas Sci Technol. https://doi.org/10.1088/1361-6501/aa9e19

23. Finazzi V, Demir AG, Biffi CA, Migliavacca F, Petrini L, Previtali B (2020) Design and functional testing of a novel balloon-expandable cardiovascular stent in CoCr alloy produced by selective laser melting. J Manuf Process 55:161–173. https://doi.org/10.1016/j.jmapro.2020.03.060

24. Yadroitsev I, Bertrand P, Antonenkova G, Grigoriev S, Smurov I (2013) Use of track/layer morphology to develop functional parts by selective laser melting. J Laser Appl 25:052003. https://doi.org/10.2351/1.4811838

25. Mandal V, Sharma S, Singh SS, Ramkumar J (2022) Laser surface texturing in powder bed fusion: numerical simulation and experimental characterization. Met Mater Int 28:181–196. https://doi.org/10.1007/s12540-021-01072-w

26. Menter FR, Kuntz M, Langtry R (2003) Ten years of industrial experience with the SST turbulence model

27. Rao H, Giet S, Yang K, Wu X, Davies CHJ (2016) The influence of processing parameters on aluminium alloy A357 manufactured by Selective Laser Melting. Mater Des 109:334–346. https://doi.org/10.1016/j.matdes.2016.07.009

28. Aversa A, Lorusso M, Trevisan F, Ambrosio E, Calignano F, Manfredi D, Biamino S, Fino P, Lombardi M, Pavese M (2017) Effect of process and post-process conditions on the mechanical properties of an A357 alloy produced via laser powder bed fusion. Metals (Basel) 7:68. https://doi.org/10.3390/met7020068

29. Pereira JC, Gil E, Solaberrieta L, Sebastián MS, Bilbao Y, Rodríguez PP (2020) Comparison of AlSi7Mg06 alloy obtained by selective laser melting and investment casting processes: Microstructure and mechanical properties in as-built/as-cast and heat-treated conditions. Mater Sci Eng A. https://doi.org/10.1016/j.msea.2020.139124

30. Speranza N, Kidd B, Schultz MP, Viola IM (2019) Modelling of hull roughness. Ocean Eng 174:31–42. https://doi.org/10.1016/j.oceaneng.2019.01.033

31. Flack KA, Schultz MP (2010) Review of hydraulic roughness scales in the fully rough regime. J Fluids Eng. https://doi.org/10.1115/1.4001492

32. Schultz MP (2002) The relationship between frictional resistance and roughness for surfaces smoothed by sanding. J Fluids Eng Trans ASME 124:492–499. https://doi.org/10.1115/1.1459073

33. Nikuradse J (1950) Laws of flow in rough pipes